Materials Advances

ROYAL SOCIETY OF CHEMISTRY

PAPER

View Article Online
View Journal | View Issue

Cite this: *Mater. Adv.*, 2023, 4, 6358

Aza-benzannulated-perylenebisimide-porphyrin dyad as an intensely absorbing donor in bulk-heterojunction organic solar cells†

Ayushi Kaushik, [a] Subhrajyoti Bhandary, [b] Ganesh D. Sharma *[c] and Jeyaraman Sankar *[a]

Received 28th August 2023,
Accepted 30th October 2023

DOI: 10.1039/d3ma00610g

rsc.li/materials-advances

Porphyrins (PORPs) have demonstrated excellent photovoltaic performances in organic solar cells when applied in combination with suitable acceptors in molecular donor–acceptor (D–A) dyads. Perylenebisimides (PBIs) have emerged as important non-fullerene acceptors, and various derivatives of PBIs have been incorporated in D–A motifs as acceptors. In this work, we describe the design and photovoltaic performance of a novel *N*-benzannulated perylenebisimide-porphyrin dyad and its Zn(II) complex. Single-crystal X-ray diffraction (SCXRD) structures show a non-coplanar arrangement between the individual chromophores in the freebase dyad. The PBI and PORP chromophoric units show head-to-tail intermolecular π–π stacking interactions with a D–A distance of 3.4 Å. Solution-processed bulk heterojunction (BHJ) organic solar cells were fabricated using each of the two synthesized molecules as donors with $PC_{71}BM$ as the acceptor. The power conversion efficiencies (PCEs) for **PDPP** and **Zn-PDPP** were 7.25% and 9.10%, respectively, and they possess significant electron and hole mobilities.

Introduction

Organic solar cells (OSCs) based on a bulk heterojunction (BHJ) active layer are thriving as one of the promising technologies for renewable energy because of their potential low-cost fabrication, mechanical flexibility, lightweight, and color-tunable features.[1–5] With the emergence of non-fullerene small molecule acceptors, the power conversion efficiency (PCE) of OSCs has exceeded 19% *via* optimizing the device structure and morphology of the BHJ active layer using polymers as a donor.[6–9] However, the application of polymer donors is significantly limited by their inherent properties, such as dispersive molecular weight and limited reproducibility, thereby leaving several challenges for the commercialization of OSCs based on polymers as donors. Therefore, it is crucial to develop a successful replacement for polymer-based BHJ-OSCs that is effective, mechanically and electronically flexible, chemically durable, and economically viable, to allow the enhancement of the PCE along with better electron mobility. Solution-processed BHJ all small molecule-OSCs have attracted renewed interest owing to their well-defined chemical structure, easy purification, and easier energy level adjustment. They could overcome the shortcoming of polymers and have emerged as promising candidates for commercial production of OSCs.[10–12] So far, the best PCEs of 11%[13–15] and 16–17%,[16–21] respectively, have been reported for all small molecule-OSCs based on fullerene and non-fullerene acceptors, which is comparable to those of polymers. Therefore, it is necessary to design simple and low-cost small molecule donors that will be compatible with both fullerene and non-fullerene acceptors for OSCs.

Rylene diimides are an important class of compounds exhibiting a variety of applications in modern organic material-based devices. These molecules possess a rigid polyaromatic backbone, along with two imide groups positioned at the edge of their long axis. The imide substituents help in the solubility of these molecules and often do not influence the electronic properties due to the presence of nodes passing through the N–N axis.[22] This class of molecules has also been extensively explored as a multi-redox system for modern optoelectronic applications.[23] Perylenebisimides (PBIs) are one of the popular members of this family due to their chemical and photochemical stability. Their photophysical characteristics make them efficient materials suitable for organic photovoltaics and organic light-emitting devices.[24] However, the narrow range of absorption of these materials needs to be improved to

[a] *Department of Chemistry, Indian Institute of Science Education and Research, Bhopal (MP) 462066, India*
[b] *Department of Chemistry, Ghent University, 9000 Ghent, Belgium*
[c] *Department of Physics and Electronics and Communication Engineering, The LNM Institute of Information Technology, Jamdoli, Jaipur (Raj), 302031, India. E-mail: gdsharma273@gmail.com, gdsharma@lnmiit.ac.in*

† Electronic supplementary information (ESI) available. CCDC 2255971 and 2255973. For ESI and crystallographic data in CIF or other electronic format see DOI: https://doi.org/10.1039/d3ma00610g

enhance their photovoltaic efficiency. Thus, developing newer derivatives of these compounds has been an active area of research in recent years.

The absorption characteristics of PBIs can be effectively tuned by functionalizing them at the available polyaromatic positions. Functionalization at the bay positions of PBIs has shown potential in influencing their electronic nature and thus dictating the photophysical properties effectively. The bay positions have been utilized for both π-extension and for π-expansion, depending on the nature of the application. The π-extension strategy has been widely exploited to achieve molecules with bathochromically shifted absorption, whereas π-expansion often results in a hypsochromic shift. However, neither method results in a panchromatic absorption ideal for applications such as artificial light harvesting. Thus, having only a PBI unit will not be sufficient to achieve this goal, but connecting a suitable accessory chromophore can augment the absorption profile. Also, the formation of optimal film morphologies for effective charge separation and transport in optoelectronics is severely hampered by the high tendency of large coplanar molecular structures for PBIs to form microscale aggregates, which significantly limits their photovoltaic performance.[25–28] Different methods have been developed to reduce intermolecular interactions and excessive domain sizes in an effort to solve this issue.[29,30] The most popular technique is to attach a bulky substituent at the bay position, which can thereby render the PBI derivatives non-planar. This aids in reducing excessive intermolecular contact and preventing the creation of large aggregates.

The π-conjugation extension strategy has been successfully used to achieve molecular platforms that have panchromatic absorption (Chart 1). One of the efficient accessory chromophores exploited for this is porphyrin, due to its complementing absorption profile with that of PBIs. Porphyrins have intense Soret bands (~400 nm) and Q-bands (~500–600 nm).[31,32] Derivatives achieved *via* conjugation extension of PBIs with ethynyl porphyrins have wider absorption profiles and have been demonstrated to show impressive performance as active layers in organic solar cells.[33,34] This is due to the electronic complementarity of the two chromophores and their absorption profiles. However, the concept of an accessory chromophore has not been explored with π-expanded PBIs for OSCs. This strategy may result in derivatives having entirely new electronic and photophysical characteristics, which will be interesting for our desired light-harvesting applications.

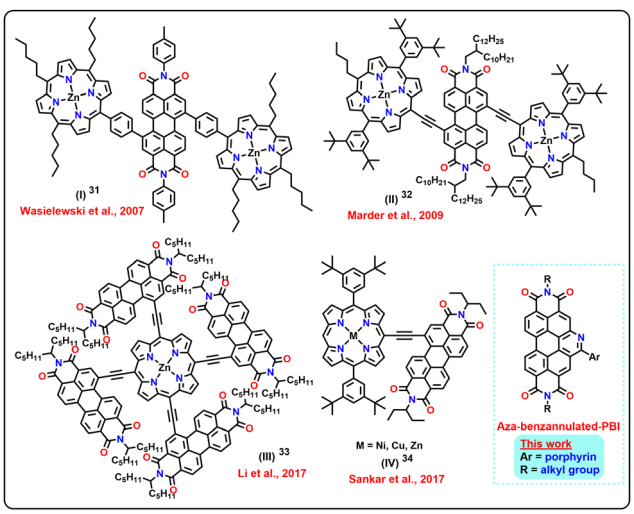

Chart 1 Selected examples of PBI-porphyrin conjugates reported and the current work.

Recently, there have been a few interesting reports on organic solar cells based on PBI and PORP with moderate PCEs; however, achieving higher efficiency is still challenging. Therefore, developing novel PORP-PBI-based small molecules with versatile structures and further obtaining insight into their potential photovoltaic application has aroused our interest. Inspired by the strategy for constructing low-bandgap materials with a D–A system, herein, the highly functionally flexible PORP platform was selected for developing D–A structural small molecule-based wide-range absorbing donors. In our previously reported work (molecule IV, Chart 1), even though the porphyrin and PBI were linked through an ethynyl bridge to incorporate electronic coupling, the performance was limited to 6% PCE. In this case, an effective charge-transfer between the donor and acceptor motifs widened the absorption range and thus provided a panchromatic absorption.[34] Despite this, the PCE could not be further improved upon. This result hinted at screening different PBI derivatives as acceptors while retaining the porphyrin as a donor to check the effect on the PCE. In this direction, it was presumed that a core-expanded PBI would be an interesting candidate to investigate the effect of anchoring with porphyrin. Additionally, the presence of a heteroatom, if any, in the core would also perturb the electronic nature of the derivative. In this direction, it was decided to link an aza-benzannulated-PBI to the *meso*-position of both a freebase porphyrin and its zinc(II) complex.

Aza-benzannulated PBIs can be obtained by simple Pictet–Spengler reaction (PSR) of 1-amino-PBI with the respective aryl aldehydes in the presence of an acid, followed by aromatization. Even though PSR is known on simple PBIs[35–38] and porphyrins individually[39,40] there is no report on connecting the two chromophores using this strategy. We report the first successful synthesis of a porphyrin-appended aza-benzannulated-PBI using a one-pot, one-step PSR, along with its zinc metal complex, in high yields. This molecular platform is also unique due to two large polyaromatic units connected directly to each other; an N-doped semicoronene diimide and a porphyrin. Most importantly, the resultant dyad is structurally characterized, and its photophysical properties are investigated. Light harvesting efficiency was investigated for the OSCs fabricated from these dyads as donors.

Results and discussion

The starting materials 1-amino-perylenebisimide (**PBN**) and 10,20-bis(3,5-ditertbutylphenyl)-porphyrin-5-carboxaldehyde (**PCHO**) were synthesized from **PBI** and **PORP**, respectively,

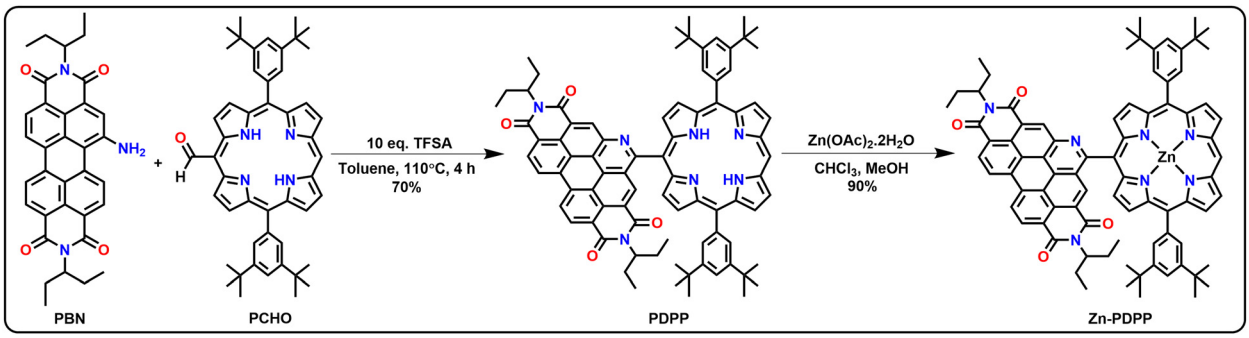

Scheme 1 Synthesis of the aza-benzannulated-PBI-porphyrin dyad (**PDPP**) and its Zn-complex (**Zn-PDPP**).

using reported procedures.[41,42] The desired molecular dyad **PDPP** was synthesized *via* a modified Pictet–Spengler condensation reaction of **PBN** and **PCHO** using trifluoromethanesulphonic acid (TFSA) as a catalyst in toluene (Scheme 1). Here, the selection of porphyrin aldehyde as one of the substrates and TFSA behaving as a reagent made this reaction happen in a single step. For the preparation of the dyad **PDPP**, two equiv. of the compound **PCHO** were taken with ten equiv. of TFSA with respect to one equivalent of **PBN** in toluene, and the reaction mixture was stirred and heated for 4 h at 110 °C under argon. No further dilution or exposure to visible light or addition of oxidant was required. The desired product was obtained with a good yield. The Zn(II)-complex was obtained by carrying out metalation of the freebase dyad using zinc acetate as shown in Scheme 1. All the PBI- and PORP-based precursors were characterized by NMR spectroscopy and mass spectrometry. Synthesis and characterization details are given in detail in the ESI† (Fig. S1–S37). The mechanistic pathway for the formation of **PDPP** in a single step is shown in Fig. S49 (ESI†).

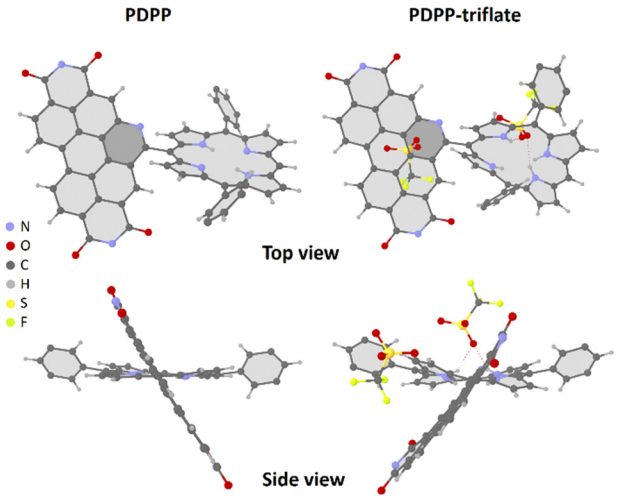

Fig. 1 SCXRD structures of **PDPP** (CCDC 2255973†) and **PDPP-triflate** (CCDC 2255971†) salt (**PDPP** crystallized using triflic acid). Alkyl chains are omitted for clarity.

Crystallography

The single-crystal X-ray diffraction studies were carried out for **PDPP** and **PDPP-triflate**. Crystals suitable for diffraction were obtained by slow-diffusion of hexane into a toluene solution and chloroform solution for **PDPP** and **PDPP-triflate**, respectively. The PBI and PORP units in the dyad **PDPP-triflate** were found to be non-coplanar with a dihedral angle of 59.4°. The core of the porphyrin was found to be ruffled in the case of the triflate salt of **PDPP** (Fig. 1). The same is the case with the crystals obtained for free-base **PDPP**. The two chromophoric units are almost orthogonal to each other with π–π stacking between the donor and the acceptor in the case of **PDPP**, as shown in Fig. 1 and Fig. S47 (ESI†).

Photophysical studies

Fig. 2a shows the absorption profiles for both the synthesized molecules in toluene. The dyad **PDPP** shows an absorption-maximum with the Soret band at 417 nm superimposing with absorption for *N*-benzannulated-PBI at around 467 nm, whereas its zinc(II) complex shows slightly red-shifted Soret and Q-bands. The emission spectra for these molecules were also recorded in toluene. It was found that the dyad **PDPP** showed a dual emission with PBI and porphyrin-based emission bands of reduced intensities (Fig. S38b, ESI†), whereas **Zn-PDPP** was non-emissive. Complete optical spectroscopic data are listed in Table 1. The absorption profiles confirm the limited electronic coupling in the ground state between the PBI and PORP units in both **PDPP** and **Zn-PDPP**. This results from the free rotation around the single bond that connects both and the non-coplanar arrangement of the two chromophores. Moreover, the PBI core in the dyads is expected to be comparatively less electron-deficient than the parent PBI (**PBI**) and thus have a reduced inductive effect on the PORP unit. The absence of any prominent CT bands in the bathochromic region further reiterates this inference. Interestingly, both the dyads possess similar molar extinction coefficients and thus hint at a marginal electronic effect by Zn(II) insertion.

The thin film UV-visible absorption spectra of both the molecules along with the absorption spectra of $PC_{71}BM$ are shown in Fig. 2b. As compared to the absorption spectra in solution, the absorption spectra in the film get broadened and redshifted due to the intermolecular interactions present in the

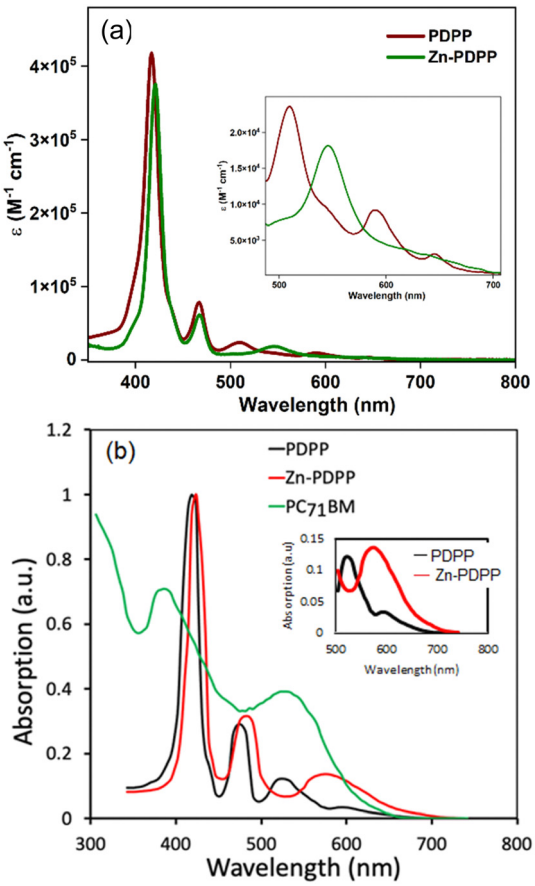

Fig. 2 UV-visible absorption spectra of **PDPP** and **Zn-PDPP** (in toluene solvent, concentration = 1 μM) (a) and in a thin film cast from chloroform solution (b). The thin film absorption spectrum of $PC_{71}BM$ is also shown in (b).

solid state. The redshift for **Zn-PDPP** is more as compared to that of **PDPP**, which is ascribed to a stronger intermolecular interaction due to the electron-rich Zn–porphyrin unit. The optical bandgaps estimated from the onset edge of these spectra are about 1.75 and 1.66 eV for **PDPP** and **Zn-PDPP**, respectively. The thin film absorption spectrum of $PC_{71}BM$ is complementary to both the synthesized molecules.

Electrochemical studies

The electrochemical properties of these new molecules were investigated by cyclic voltammetry (CV) in deaerated CH_2Cl_2 using Bu_4NPF_6 (TBAP) as a supporting electrolyte (Fig. 3). The dyad **Zn-PDPP** shows three reversible reductions and two reversible oxidations. In contrast, **PDPP** shows two irreversible oxidations along with three reversible reductions. Out of these,

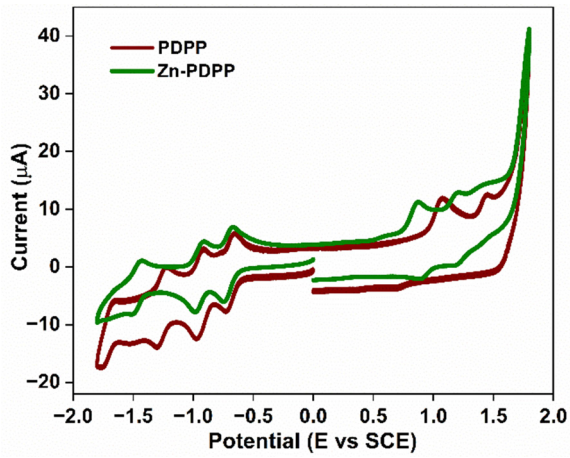

Fig. 3 Cyclic voltammograms (CV) for **PDPP**, and **Zn-PDPP** in TBAP (0.1 M), and CH_2Cl_2 at 100 mV s^{-1}.

the first two reductions are expected to be PBI-centered, while the third one corresponds to a porphyrin-centered reduction. The two oxidations were expected to be of porphyrin type in each case. Further details on the reduction and oxidation potentials and electrochemical band gaps for these molecules are given in Table 1. The HOMO/LUMO energy levels obtained from electrochemical investigations are −5.44/−3.72 and −5.23/−3.66 eV, for **PDPP** and **Zn-PDPP**, respectively.

The LUMO offsets between **PDPP** or **Zn-PDPP** and $PC_{71}BM$ (LUMO = −4.12 eV) are about 0.30 or 0.38 eV, greater than the driving force needed for exciton dissociation and charge separation in the BHJ active layer.

Density functional theory (DFT) calculations

To visualize the electron delocalization, DFT calculations were carried out at the B3LYP/6-31g(d,p) level using the Gaussian 09 suite of programs for the dyads. The HOMOs and LUMOs for both molecules are shown in Fig. 4. The HOMO was found to be localized mainly on the porphyrin core while the LUMO was found to be localized over the PBI core along with its N-heteroring in each case. This is in line with the expectation for the individual chromophores.

Photovoltaic properties

The conventional BHJ-OSCs were fabricated with a structure of ITO/PEDOT:PSS/**PDPP** or **Zn-PDPP**:$PC_{71}BM$/PFN/Al. The targeted BHJ active layer consisted of **PDPP** or **Zn-PDPP** as the donor and $PC_{71}BM$ as the acceptor prepared by spin coating the blend solution of the donor and acceptor with different D/A weight ratios in chloroform solution and it was found that the

Table 1 Optical and electrochemical data for **PDPP** and **Zn-PDPP** in toluene

Comp	λ_{abs}^{max} (nm)	$\lambda_{abs}^{max\,b}$ (nm)	ε (M^{-1} cm^{-1})	E_{opt} (eV)	HOMO[a] (eV)	LUMO[a] (eV)	E_g[a] (eV)
PDPP	417	478	417 000	1.84	−5.44	−3.72	1.72
Zn-PDPP	421	486	376 000	1.74	−5.23	−3.66	1.57

[a] Obtained from electrochemical measurements carried out in dichloromethane. [b] Values obtained from thin-film.

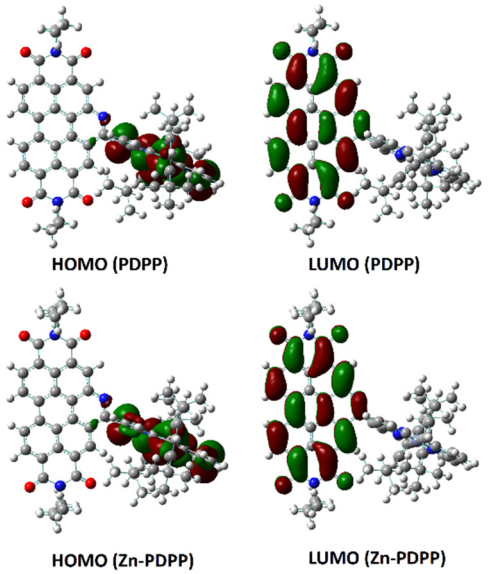

Fig. 4 Frontier molecular orbitals of **PDPP** and **Zn-PDPP** obtained by DFT, calculated at the B3LYP/6-31G(d,p) level.

ratio with 1 : 1.4 showed the best photovoltaic performance. To optimize the morphology of the BHJ active layer and to improve the photovoltaic performance, pyridine as the solvent additive was added to the chloroform solution (0.5 v%) prior to the spin coating process, it was found that the power conversion efficiency was improved after this modification. To improve the photovoltaic performance further, we have adopted solvent vapor treatment by exposing the optimized active layer with THF vapour for 40 s, before the deposition of the PFN layer. The current–voltage characteristics of the OSCs are presented in Fig. 5a and the corresponding photovoltaic parameters are summarized in Table 2. The optimized OSCs based on **PDPP** and **Zn-PDPP** showed overall PCEs of 7.25% and 9.10%, respectively. The OSC based on **PDPP** showed a higher value of V_{OC} (0.94 V) than its **Zn-PDPP** counterpart owing to the deeper HOMO energy level of **PDPP**, the enhanced value of the PCE for **Zn-PDPP**-based OSCs is due to the improved values of both current density (J_{SC}) and fill factor (FF).

Table 2 Photovoltaic parameters of the optimized OSCs using **PDPP** and **Zn-PDPP** as the donor and $PC_{71}BM$ as the acceptor

Donor	J_{SC} (mA cm^{-2})	V_{OC} (V)	FF	PCE (%)
PDPP	13.08	0.94	0.59	7.25 (7.04)[a]
Zn-PDPP	17.28	0.81	0.65	9.10 (8.94)[a]

[a] Average of 8 devices.

The higher value of J_{SC} for the **Zn-PDPP**-based OSCs may be attributed to its lower optical bandgap as compared to **PDPP**, which is beneficial for high exciton generation in the former OSC than the latter.

Furthermore, the external quantum efficiency (EQE) of the OSCs was measured as shown in Fig. 5b. As presented in Fig. 5b, the EQE spectra of the OSCs closely resemble the corresponding absorption spectra of the active layers (Fig. 2b). The EQE spectra for **Zn-PDPP** are extended up to 760 nm whereas for the **PDPP** counterpart it is limited up to 720 nm. These results suggest that the light-harvesting efficiency in the **Zn-PDPP**-based OSC is higher than that of the **PDPP** counterpart. The J_{SC} values estimated from the integration of the EQE spectra are about 12.76 and 17.04 mA cm^{-2} for **PDPP** and **Zn-PDPP**-based OSCs, respectively, and this trend agrees with the values obtained from the *J–V* curves under illumination.

The exciton generation and their subsequent dissociation into free charge carriers, and the charge transport and recombination processes within the active layer, play a crucial role in the overall PCE. To get information about the exciton generation and their dissociation into free charge carriers, the variation of photocurrent density (J_{ph}) with effective voltage (V_{eff})[43,44] was investigated and shown in Fig. 6. The J_{ph} is estimated as $J_{ph} = J_L - J_D$, where J_L and J_D are the current densities under illumination and in the dark, respectively and $V_{eff} = V_o - V_a$, where V_o is the voltage when J_{ph} is zero, and V_a is the applied voltage.

In general, when V_{eff} is increased to a sufficiently high value, the J_{ph} is independent of V_{eff}, and reached its saturation value (J_{sat}) and only depends upon the light harvesting efficiency of the active layer. The maximum exciton generation rate (G_{max})

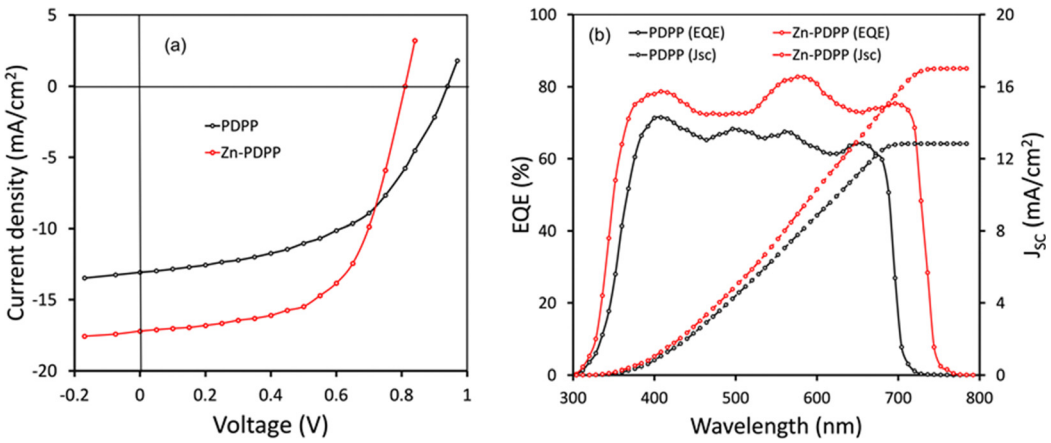

Fig. 5 (a) *J–V* Characteristics under illumination (AM1.5 G. 100 mW cm^{-2}) and EQE spectra of OSCs. Estimated values of J_{SC} are also shown in (b).

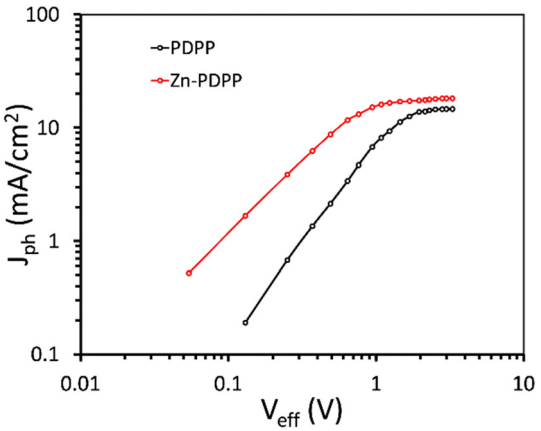

Fig. 6 Variation of J_{ph} with V_{eff} for OSCs.

can be estimated as G_{max}= J_{sat}/qL, where q is the elementary charge and L is the thickness of the active layer and is about 0.96×10^{28} m^{-3} s^{-1}, and 1.15×10^{28} m^{-3} s^{-1} for **PDPP**:$PC_{71}BM$ and **Zn-PDPP**:$PC_{71}BM$ based OSCs, respectively, indicating that more excitons are generated in the latter device as compared to the former one. The values of exciton dissociation probability (P_{diss}) and charge collection probability (P_{coll}) were estimated as the ratio of J_{ph}/J_{sat} under short circuit conditions and maximum power conditions, respectively. The values of P_{diss}/P_{coll} for the **PDPP**:$PC_{71}BM$ and **Zn-PDPP**:$PC_{71}BM$ are about 0.886/0.667 and 0.942/0.712, respectively. It can be seen from Fig. 6 that the J_{ph} saturates at a higher value of V_{eff} for **PDPP**:$PC_{71}BM$ than for **Zn-PDPP**:$PC_{71}BM$, indicating that more effective internal electric field is needed to sweep the charge carriers towards the electrode for the former than the latter. These observations indicate that the G_{max}, P_{diss} and P_{coll} are higher for **Zn-PDPP**:$PC_{71}BM$ than for **PDPP**:$PC_{71}BM$, which may be one of the origins for the higher values of both J_{SC} and FF for the former.

To get information about the charge transport, we have prepared hole only devices (ITO/PEDOT:PSS/active layer/Au) and electron only devices (ITO/Al/active layer/Al) and measured their dark J–V characteristics. We have fitted these curves with space-charge limited current (SCLC) to estimate the hole mobility (μ_h) and electron mobility (μ_e)[45] (Fig. 7). The values of μ_e (3.12×10^{-4} cm^2 V^{-1} s^{-1}) and μ_h (2.34×10^{-4} cm^2 V^{-1} s^{-1}) for **Zn-PDPP**:$PC_{71}BM$ are higher with a μ_e/μ_h ratio of 1.33 than that for **PDPP**:$PC_{71}BM$ ($\mu_e = 3.06 \times 10^{-4}$ cm^2 V^{-1} s^{-1} and $\mu_h = 2.02 \times 10^{-4}$ cm^2 V^{-1} s^{-1} with μ_e/μ_h = 1.51), indicating that the charge transport in the former device is more efficient than the latter, resulting in high value of FF for **Zn-PDPP**:$PC_{71}BM$-based OSCs. Here, $V - V_{bi}$ (in volts) on the horizontal axis in Fig. 7 represents the difference in the applied voltage (V) and built-in potential (V_{bi}).

We have examined the variation of J_{SC} and V_{OC} with illumination intensity (P_{in}) for these devices,[46,47] as shown in Fig. 8. The variation of J_{SC} with P_{in} follows the power law as $J_{SC} \propto (P_{in})\alpha$, where α is the exponent power factor and gives information about the degree of bimolecular recombination. When the value of α is unity, the bimolecular recombination is almost negligible, whereas if the value of α is less than unity, it indicates the occurrence of bimolecular recombination in the active layer. The value of α for the devices based on **Zn-PDPP** is higher (0.939) compared to those based on **PDPP** (0.881), indicating that the bimolecular recombination is suppressed for the former device as compared to the latter one. The variation of V_{OC} with P_{in} follows the relationship as $V_{OC} = (nkT/q)\ln(P_{in})$, where k is Boltzmann's constant, T is the absolute temperature, q is the elementary charge, and n is the diode quality factor. The value of n estimated from the slope of the V_{OC}–P_{in} curves is about 1.46 and 1.31 for **PDPP** and **Zn-PDPP**-based devices, indicating that the trap-assisted recombination is more suppressed for the **Zn-PDPP**-based OSCs, compared to the **PDPP** counterpart. The reduced bimolecular and trap-assisted recombination for **Zn-PDPP**-based-OSCs lead to higher values of both J_{SC} and FF.

To gain further information about the charge carrier dynamics process in these OSCs, transient photocurrent (TPC) and transient photovoltage (TPV) decays were measured and shown in Fig. 9. The charge carrier lifetime and extraction time were derived from the TPV and TPC decay curves,

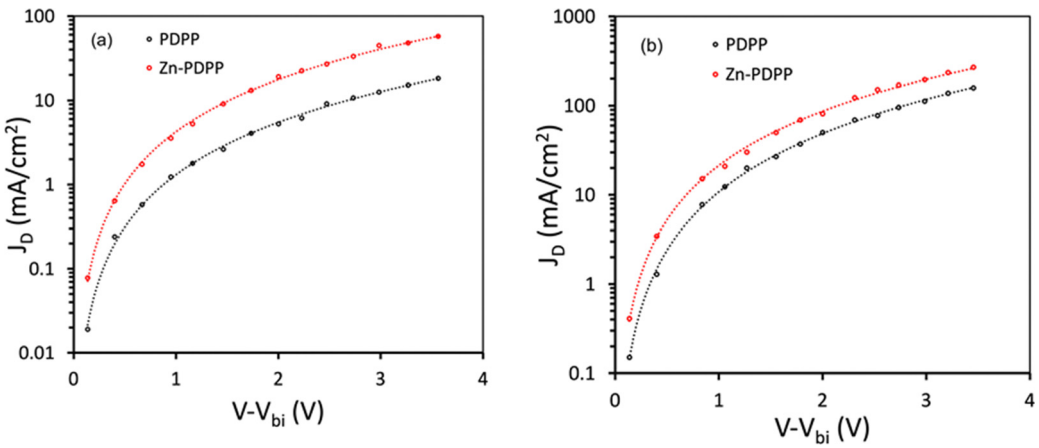

Fig. 7 Dark J–V characteristics for (a) hole-only and (b) electron-only devices and SCLC fitting.

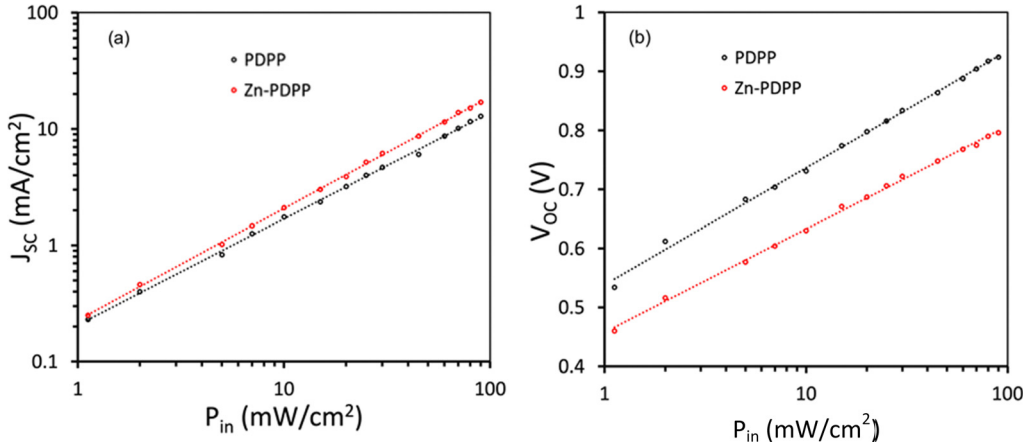

Fig. 8 Variation of (a) J_{SC} and (b) V_{OC} for the OSCs.

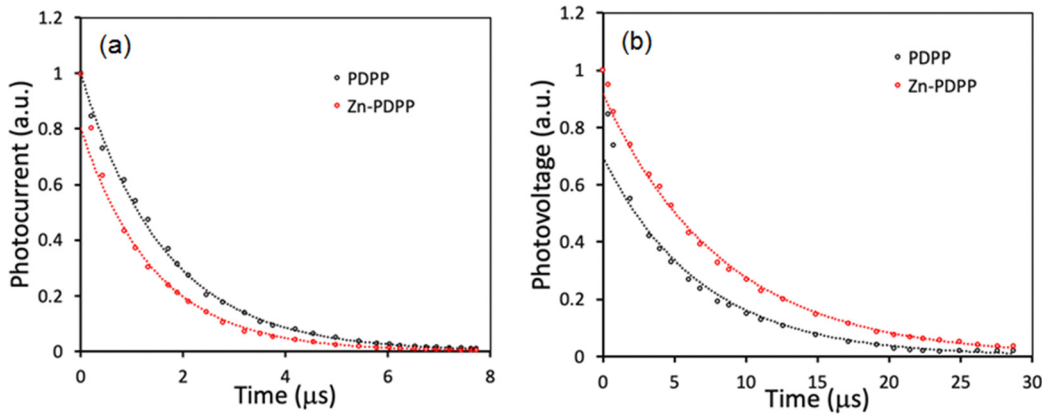

Fig. 9 (a) Transient photocurrent and (b) transient photovoltage decay curves for OSCs.

respectively, using mono-exponential fits.[48,49] The device based on **Zn-PDPP** showed shorter extraction time (1.41 s) than the **PDPP** counterpart (1.63 s) estimated from the TPC curves (Fig. 9a), indicating more efficient extraction of the charge carriers in the former device than the latter, which is in good agreement with the higher value of charge collection probability (P_{coll}). As shown in Fig. 9b, the charge carrier lifetimes estimated from the TPV decay curves in the device based on **PDPP** and **Zn-PDPP** are 7.09 s and 8.36 s, respectively. The relatively longer charge carrier time in the **Zn-PDPP**-based device than the **PDPP** counterpart implies that significantly reduced charge recombination occurred in the former device than the latter, which is in good agreement with the higher value of FF.[50]

Conclusion

We present here a one-step synthesis for N-doped semicoronene diimides using a strong acid for its application as an intensely absorbing donor in organic photovoltaic devices. The current study confirms that the novel PBI-PORP dyad is a new and promising donor platform for BHJ-OSCs. In solution-processed small-molecule OSCs, the free-base and the zinc-metallated dyads demonstrated good photovoltaic performances when used as donors against $PC_{71}BM$ as the acceptor. The photovoltaic studies revealed an overall PCE of 7.25% and 9.10% for **PDPP** and **Zn-PDPP**, respectively, after optimizing the donor-to-acceptor weight ratio (1 : 1.4), which is much higher than that of the previously reported PBI-PORP dyads. Solvent vapor treatment is expected to improve the nanoscale morphology of the active layer, which is necessary for exciton formation and their dissociation into free charge carriers. The above findings imply that the novel PBI-PORP dyads are potential motifs in low-cost organic photovoltaic cells and can be employed to fabricate highly efficient solar cells.

Author contributions

AK synthesized and characterized all the molecules and analyzed the spectral data. SB solved the SCXRD data. GD and JS supervised and co-wrote the manuscript. All the authors have consented to the contents of the manuscript.

Conflicts of interest

There are no conflicts to declare.

Acknowledgements

The authors sincerely acknowledge DST-SERB-EMR/2016/005768 and DST-SERB-CRG/2020/004632 for the financial support. The facilities and infrastructure provided by IISER Bhopal are highly acknowledged. AK is thankful to IISER Bhopal for a senior research fellowship.

Notes and references

1 W. Lowrie, R. J. E. Westbrook, J. Guo, H. I. Gonev, J. Marin-Beloqui and T. M. Clarke, *J. Chem. Phys.*, 2023, **158**, 110901.
2 G. Zhang, F. R. Lin, F. Qi, T. Heumüller, A. Distler, H. J. Egelhaaf, N. Li, P. C. Y. Chow, C. J. Brabec, A. K. Y. Jen and H. L. Yip, *Chem. Rev.*, 2022, **122**, 14180–14274.
3 H. Yao and J. Hou, *Angew. Chem., Int. Ed.*, 2022, **61**, e202209021, DOI: **10.1002/anie.202209021**.
4 B. Zhang, F. Yang and Y. Li, *Small Sci.*, 2023, **3**, 2300004, DOI: **10.1002/smsc.202300004**.
5 Y. Li, G. Xu, C. Cui and Y. Li, *Adv. Energy Mater.*, 2018, **8**, 1–28.
6 L. Zhu, M. Zhang, J. Xu, C. Li, J. Yan, G. Zhou, W. Zhong, T. Hao, J. Song, X. Xue, Z. Zhou, R. Zeng, H. Zhu, C. C. Chen, R. C. I. MacKenzie, Y. Zou, J. Nelson, Y. Zhang, Y. Sun and F. Liu, *Nat. Mater.*, 2022, **21**, 656–663.
7 D. Li, N. Deng, Y. Fu, C. Guo, B. Zhou, L. Wang, J. Zhou, D. Liu, W. Li, K. Wang, Y. Sun and T. Wang, *Adv. Mater.*, 2023, **35**, 1–9.
8 T. Gokulnath, J. Kim, H. Kim, J. Park, D. Song, H. Y. Park, R. Kumaresan, Y. Y. Kim, J. Yoon and S. H. Jin, *ACS Appl. Mater. Interfaces*, 2023, **15**, 19307–19318, DOI: **10.1021/acsami.3c01121**.
9 J. Fu, P. W. K. Fong, H. Liu, C. S. Huang, X. Lu, S. Lu, M. Abdelsamie, T. Kodalle, C. M. Sutter-Fella, Y. Yang and G. Li, *Nat. Commun.*, 2023, **14**, 1760.
10 S. D. Collins, N. A. Ran, M. C. Heiber and T. Q. Nguyen, *Adv. Energy Mater.*, 2017, **7**, 1602242, DOI: **10.1002/aenm.201602242**.
11 H. Gao, Y. Sun, L. Meng, C. Han, X. Wan and Y. Chen, *Small*, 2023, **19**, 2205594, DOI: **10.1002/smll.202205594**.
12 B. Kan, Y. Kan, L. Zuo, X. Shi and K. Gao, *InfoMat*, 2021, **3**, 175–200.
13 B. Kan, Q. Zhang, M. Li, X. Wan, W. Ni, G. Long, Y. Wang, X. Yang, H. Feng and Y. Chen, *J. Am. Chem. Soc.*, 2014, **136**, 15529–15532.
14 D. Deng, Y. Zhang, J. Zhang, Z. Wang, L. Zhu, J. Fang, B. Xia, Z. Wang, K. Lu, W. Ma and Z. Wei, *Nat. Commun.*, 2016, **7**, 1–9.
15 J. Wan, X. Xu, G. Zhang, Y. Li, K. Feng and Q. Peng, *Energy Environ. Sci.*, 2017, **10**, 1739–1745.
16 J. Ge, L. Hong, H. Ma, Q. Ye, Y. Chen, L. Xie, W. Song, D. Li, Z. Chen, K. Yu, J. Zhang, Z. Wei, F. Huang and Z. Ge, *Adv. Mater.*, 2022, **34**, 1–9.
17 J. Qin, Z. Chen, P. Bi, Y. Yang, J. Zhang, Z. Huang, Z. Wei, C. An, H. Yao, X. Hao, T. Zhang, Y. Cui, L. Hong, C. Liu, Y. Zu, C. He and J. Hou, *Energy Environ. Sci.*, 2021, **14**, 5903–5910.
18 Y. Sun, L. Nian, Y. Kan, Y. Ren, Z. Chen, L. Zhu, M. Zhang, H. Yin, H. Xu, J. Li, X. Hao, F. Liu, K. Gao and Y. Li, *Joule*, 2022, **6**, 2835–2848.
19 Y. Gao, X. Yang, W. Wang, R. Sun, J. Cui, Y. Fu, K. Li, M. Zhang, C. Liu, H. Zhu, X. Lu and J. Min, *Adv. Mater.*, 2023, **2300531**, 1–11.
20 W. Gao, M. Jiang, Z. Wu, B. Fan, W. Jiang, N. Cai, H. Xie, F. R. Lin, J. Luo, Q. An, H. Y. Woo and A. K. Y. Jen, *Angew. Chem., Int. Ed.*, 2022, **61**, e202205168, DOI: **10.1002/anie.202205168**.
21 X. Wang, Z. Li, X. Zheng, C. Xiao, T. Hu, Y. Liao and R. Yang, *Adv. Funct. Mater.*, 2023, 2300323.
22 F. Würthner, C. R. Saha-Möller, B. Fimmel, S. Ogi, P. Leowanawat and D. Schmidt, *Chem. Rev.*, 2016, **116**, 962–1052.
23 J. Shukla, V. P. Singh and P. Mukhopadhyay, *ChemistryOpen*, 2020, **9**, 304–324.
24 A. Nowak-Król and F. Würthner, *Org. Chem. Front.*, 2019, **6**, 1272–1318.
25 H. Wang, M. Li, Y. Liu, J. Song, C. Li and Z. Bo, *J. Mater. Chem. C*, 2019, **7**, 819–825.
26 Y. Lin, Y. Wang, J. Wang, J. Hou, Y. Li, D. Zhu and X. Zhan, *Adv. Mater.*, 2014, **26**, 5137–5142.
27 S. Y. Liu, C. H. Wu, C. Z. Li, S. Q. Liu, K. H. Wei, H. Z. Chen and A. K. Y. Jen, *Adv. Sci.*, 2015, **2**, 1–7.
28 J. Zhao, Y. Li, J. Zhang, L. Zhang, J. Y. L. Lai, K. Jiang, C. Mu, Z. Li, C. L. C. Chan, A. Hunt, S. Mukherjee, H. Ade, X. Huang and H. Yan, *J. Mater. Chem. A*, 2015, **3**, 20108–20112.
29 J. Lee, R. Singh, D. H. Sin, H. G. Kim, K. C. Song and K. Cho, *Adv. Mater.*, 2016, **28**, 69–76.
30 Y. Liu, C. Mu, K. Jiang, J. Zhao, Y. Li, L. Zhang, Z. Li, J. Y. L. Lai, H. Hu, T. Ma, R. Hu, D. Yu, X. Huang, B. Z. Tang and H. Yan, *Adv. Mater.*, 2015, **27**, 1015–1020.
31 R. F. Kelley, W. S. Shin, B. Rybtchinski, L. E. Sinks and M. R. Wasielewski, *J. Am. Chem. Soc.*, 2007, **129**, 3173–3181.
32 S. A. Odom, R. F. Kelley, S. Ohira, T. R. Ensley, C. Huang, L. A. Padilha, S. Webster, V. Coropceanu, S. Barlow, D. J. Hagan, E. W. Van Stryland, J. L. Brédas, H. L. Anderson, M. R. Wasielewski and S. R. Marder, *J. Phys. Chem. A*, 2009, **113**, 10826–10832.
33 A. Zhang, C. Li, F. Yang, J. Zhang, Z. Wang, Z. Wei and W. Li, *Angew. Chem., Int. Ed.*, 2017, **56**, 2694–2698.
34 R. Mishra, R. Regar, R. Singhal, P. Panini, G. D. Sharma and J. Sankar, *J. Mater. Chem. A*, 2017, **5**, 15529–15533.
35 L. Hao, W. Jiang and Z. Wang, *Tetrahedron*, 2012, **68**, 9234–9239.
36 M. Schulze, M. Philipp, W. Waigel, D. Schmidt and F. Würthner, *J. Org. Chem.*, 2016, **81**, 8394–8405.
37 P. Hudhomme, R. El-Berjawi, L. Rocard, A. Goujon and T. Cauchy, *J. Org. Chem.*, 2020, **85**, 12252–12261.
38 A. Goujon, L. Rocard, T. Cauchy and P. Hudhomme, *J. Org. Chem.*, 2020, **85**, 7218–7224.
39 K. Gao, N. Fukui, S. I. Jung, H. Yorimitsu, D. Kim and A. Osuka, *Angew. Chem., Int. Ed.*, 2016, **55**, 13038–13042.

40 D. K. Singh and M. Nath, *Org. Biomol. Chem.*, 2015, **13**, 1836–1845.
41 H. Y. Tsai and K. Y. Chen, *Dyes Pigm.*, 2013, **96**, 319–327.
42 K. Susumu, T. Shimidzu, K. Tanaka and H. Segawa, *Tetrahedron Lett.*, 1996, **37**, 8399–8402.
43 P. W. M. Blom, V. D. Mihailetchi, L. J. A. Koster and D. E. Markov, *Adv. Mater.*, 2007, **19**, 1551–1566.
44 V. D. Mihailetchi, L. J. A. Koster, J. C. Hummelen and P. W. M. Blom, *Phys. Rev. Lett.*, 2004, **93**, 19–22.
45 M. Sajedi Alvar, P. W. M. Blom and G. J. A. H. Wetzelaer, *Nat. Commun.*, 2020, **11**, 1–9.
46 S. Zeiske, W. Li, P. Meredith, A. Armin and O. J. Sandberg, *Cell Rep. Phys. Sci.*, 2022, **3**, 101096.
47 A. K. K. Kyaw, D. H. Wang, V. Gupta, W. L. Leong, L. Ke, G. C. Bazan and A. J. Heeger, *ACS Nano*, 2013, 4569–4577.
48 S. Wood, J. C. Blakesley and F. A. Castro, *Phys. Rev. Appl.*, 2018, **10**, 1.
49 S. Wood, D. O'Connor, C. W. Jones, J. D. Claverley, J. C. Blakesley, C. Giusca and F. A. Castro, *Sol. Energy Mater. Sol. Cells*, 2017, **161**, 89–95.
50 R. Yu, H. Yao, Y. Cui, L. Hong, C. He and J. Hou, *Adv. Mater.*, 2019, **31**, 1–8.